BREAK

A TIME-LINEARIZED NAVIER–STOKES ANALYSIS OF STALL FLUTTER

William S. Clark[*] and Kenneth C. Hall[†]
Department of Mechanical Engineering and Materials Science
Duke University
Durham, North Carolina

ABSTRACT

A computational method for accurately and efficiently predicting unsteady viscous flow through two-dimensional cascades is presented. The method is intended to predict the onset of the aeroelastic phenomenon of stall flutter. In stall flutter, viscous effects significantly impact the aeroelastic stability of a cascade. In the present effort, the unsteady flow is modeled using a time-linearized Navier-Stokes analysis. Thus, the unsteady flow field is decomposed into a nonlinear spatially varying mean flow plus a small-perturbation harmonically varying unsteady flow. The resulting equations that govern the perturbation flow are linear, variable coefficient partial differential equations. These equations are discretized on a deforming, multi-block, computational mesh and solved using a finite-volume Lax-Wendroff integration scheme. Numerical modelling issues relevant to the development of the unsteady aerodynamic analysis, including turbulence modelling, are discussed. Results from the present method are compared to experimental stall flutter data, and to a non-linear time-domain Navier–Stoke analysis. The results presented demonstrate the ability of the present time-linearized analysis to model accurately the unsteady aerodynamics associated with turbomachinery stall flutter.

1. INTRODUCTION

Turbomachinery stall flutter is an aeroelastic instability of compressor and fan blades that often occurs near the stall or choke lines on the operating map. Stall flutter usually appears at part speeds where blades are subjected to high mean flow incidences. The vibratory frequencies associated with stall flutter generally coincide with one of the blade's lowest natural frequencies. Frequently, the mode of blade vibration corresponds to the first torsional mode. However, stall flutter can sometimes occur in the first bending mode as well.

A flutter model is composed of two parts: a structural dynamic model of the bladed-disk to predict the mode shapes and natural frequencies of the airfoil vibratory modes, and an unsteady aerodynamic model to predict the aerodynamic forces induced by airfoil vibration. While current finite element models of the structural dynamic behavior of bladed disks are quite acceptable for this application (at least for structurally tuned rotors), unsteady aerodynamic models of separated viscous flows that are both physically accurate and computationally efficient have heretofore been unavailable. Instead, designers have had to rely on empirical correlations.

In conventional stall flutter, the blade vibration is the primary fluid dynamic driver (see Sisto (1987) and Chi & Srinivasan (1985)). While significant progress has been made in the computational modelling of inviscid unsteady flows over the past 40 years, little headway has been made in modelling unsteady viscous flows, other than through direct simulation using nonlinear time-marching techniques. Unfortunately, these methods are computationally very expensive, and thus of limited use for routine design.

A number of investigators have developed time-linearized models of unsteady inviscid flows in turbomachinery. In the time-linearized approach, the flow is decomposed into a nonlinear steady flow plus a small-perturbation harmonic unsteady flow. The resulting time-linearized equations are linear variable coefficient equations that can be solved very efficiently. Verdon & Caspar (1982), Verdon (1987), Whitehead & Grant (1981), and later Hall (1993) developed time-linearized models of two-dimensional potential flow in cascades. Hall & Crawley (1989), Hall & Clark (1993), and Holmes & Chuang (1993) developed two-dimensional time-linearized Euler solvers. Hall & Lorence (1993) have developed a three-dimensional linearized Euler solver and showed that three-dimensional effects have a strong influence on unsteady flows in turbomachinery. All

---

[*] Assistant Research Professor, Department of Mechanical Engineering and Materials Science.
[†] Associate Professor, Department of Mechanical Engineering and Materials Science, Member ASME.

of these analyses are inviscid, however, and thus are not capable of predicting unsteady flows with flow separations, an important feature of stall flutter.

Recently, Clark & Hall (1995) developed a time-linearized Navier–Stokes analysis of unsteady viscous flows in cascades. They were able to predict unsteady laminar flows, including laminar separated flows, within a time-linearized framework. Furthermore, their results clearly demonstrated the destabilizing influence of viscosity (flow separation) on the aeroelastic stability of cascades, especially for torsional vibrations of the blades. However, this initial work was limited to laminar flows, and thus neglected the important role of turbulence on the unsteady flow field. More recently, Holmes & Lorence (1998) have presented a three-dimensional time-linearized Navier–Stokes analysis with a k–ω turbulence model. Their computational results, however, were limited to flows with thin attached boundary layers.

In this paper, we apply the time-linearization technique to the two-dimensional Reynolds averaged Navier–Stokes equations. The one-equation turbulence model due to Spalart & Allmaras (1992) provides the necessary closure for the Reynolds stress terms. We present computational predictions of unsteady, viscous flows resulting from torsional blade vibrations of a cascade of fan blades. The computational results from the present time-linearized Navier–Stokes method are compared to experimental data, and also to a nonlinear time-domain Navier–Stokes analysis. Two operating conditions are considered. The first condition presented corresponds to a design point on the operating line of the fan, that is, the steady flow is attached and the blades are subjected to relatively low incidence angles. The second condition corresponds to off-design operation. In this case, the blades are subjected to high incidence angles, and the steady flow separates from the blade over much of the suction surface. In both cases, numerical predictions are found to be in good agreement with the available experimental data.

2. THEORY

2.1. Governing Equations

In strong conservation law form, the two-dimensional Reynolds averaged Navier-Stokes equations are given by

$$\frac{\mathrm{d}}{\mathrm{d}t} \iint_D \mathbf{U}\,\mathrm{d}x\mathrm{d}y + \oint_{\partial D} \left(\mathbf{F} - \mathbf{U}\frac{\partial f}{\partial t} \right)\mathrm{d}y$$

$$- \oint_{\partial D} \left(\mathbf{G} - \mathbf{U}\frac{\partial g}{\partial t} \right)\mathrm{d}x = \iint_D \mathbf{S}\,\mathrm{d}x\mathrm{d}y \qquad (1)$$

where D is a deforming control volume bounded by the control surface ∂D. The quantities $\partial f/\partial t$ and $\partial g/\partial t$ are the x- and y-components of the velocity of the control surface ∂D. The vector of conservation variables $\mathbf{U}$, the flux vectors $\mathbf{F}$ and $\mathbf{G}$, and the source

vector $\mathbf{S}$ are given by

$$\mathbf{U} = \begin{bmatrix} \rho \\ \rho u \\ \rho v \\ \rho e \\ \rho \tilde{\nu} \end{bmatrix}, \quad \mathbf{F} = \begin{bmatrix} \rho u \\ \rho u^2 + p - \tau_{xx} \\ \rho uv - \tau_{xy} \\ \rho uH - \tau_{hx} \\ \rho u\tilde{\nu} - \tau_{\nu x} \end{bmatrix},$$

$$\mathbf{G} = \begin{bmatrix} \rho v \\ \rho uv - \tau_{xy} \\ \rho v^2 + p - \tau_{yy} \\ \rho vH - \tau_{hy} \\ \rho v\tilde{\nu} - \tau_{\nu y} \end{bmatrix}, \quad \mathbf{S} = \begin{bmatrix} 0 \\ 0 \\ 0 \\ 0 \\ S_t \end{bmatrix} \qquad (2)$$

The first four equations are the conservation of mass, x- and y-components of conservation of momentum, and conservation of energy, respectively. The fifth equation is the Spalart–Allmaras turbulence model written in strong conservation form.

In the above equations, ρ is the density, u and v are the velocity components in the x- and y-directions respectively, e is the total internal energy, H is the total enthalpy, and p is the static pressure. The fluid is assumed to be a perfect gas so that the total energy e is related to the total enthalpy H by

$$H = e + \frac{p}{\rho} = \frac{\gamma}{\gamma - 1}\frac{p}{\rho} + \frac{1}{2}\left(u^2 + v^2\right) \qquad (3)$$

The shear stresses τ_{xx}, τ_{xy}, and τ_{yy} are given by

$$\tau_{xx} = (\mu + \mu_t)\left(\frac{4}{3}\frac{\partial u}{\partial x} - \frac{2}{3}\frac{\partial v}{\partial y}\right) \qquad (4)$$

$$\tau_{xy} = (\mu + \mu_t)\left(\frac{\partial u}{\partial y} + \frac{\partial v}{\partial x}\right) \qquad (5)$$

$$\tau_{yy} = (\mu + \mu_t)\left(\frac{4}{3}\frac{\partial v}{\partial y} - \frac{2}{3}\frac{\partial u}{\partial x}\right) \qquad (6)$$

where μ, μ_t, and ν are the molecular viscosity, the turbulent viscosity, and the kinematic viscosity, respectively. The terms τ_{hx} and τ_{hy} in the energy equation are given by

$$\tau_{hx} = u\tau_{xx} + v\tau_{xy} - q_x \qquad (7)$$

$$\tau_{hy} = u\tau_{xy} + v\tau_{yy} - q_y \qquad (8)$$

where q_x and q_y are the x- and y-components of the heat flux, respectively, and can be written as

$$q_x = -\left(\frac{\mu c_p}{\mathrm{Pr}} + \frac{\mu_t c_p}{\mathrm{Pr}_t}\right)\frac{\partial T}{\partial x} \qquad (9)$$

$$q_y = -\left(\frac{\mu c_p}{\mathrm{Pr}} + \frac{\mu_t c_p}{\mathrm{Pr}_t}\right)\frac{\partial T}{\partial y} \qquad (10)$$

where c_p is the specific heat at constant pressure, T is the temperature, and Pr and Pr_t are the laminar and turbulent Prandtl numbers, respectively.

2

In the present study, the laminar coefficient of viscosity is determined using Sutherland's law. The turbulent viscosity is modelled using the one-equation turbulence model due to Spalart & Allmaras (1992). The turbulence model describes the convection, production, and destruction of the turbulent viscosity μ_t in terms of $\tilde{\nu}$, the working "conservation" variable, i.e.

$$\mu_t = \rho\tilde{\nu}f_{v1}(\chi) \tag{11}$$

where

$$\chi = \frac{\tilde{\nu}}{\nu}, \quad f_{v1} = \frac{\chi^3}{\chi^3 + 7.1^3} \tag{12}$$

The working variable $\tilde{\nu}$ is used in lieu of the turbulent viscosity μ_t because $\tilde{\nu}$, by construction, varies nearly linearly near the airfoil surface. The turbulent viscosity, on the other hand, varies rapidly near the airfoil surface, requiring very fine grids to resolve the laminar sublayer. Compared to some other turbulence models – e.g. k–ϵ models – which require very tight grid spacing near the airfoil surface, the Spalart–Allmaras turbulence model grid requirements are quite modest. Indeed, a computational grid with a grid spacing $\Delta y^+ = 5.0$ near the airfoil surface is acceptable.

The remaining viscous "shear" terms in the turbulence equation are given by

$$\tau_{\nu x} = \frac{1}{\lambda}\rho(\nu + \tilde{\nu})\frac{\partial\tilde{\nu}}{\partial x} \tag{13}$$

$$\tau_{\nu y} = \frac{1}{\lambda}\rho(\nu + \tilde{\nu})\frac{\partial\tilde{\nu}}{\partial y} \tag{14}$$

where λ is a constant equal to $2/3$.

Finally, the non-zero entry in the source vector S_t in Eq. (2) models the diffusion, production, and destruction of turbulence, and is a function of the local density, viscosity, the working variable $\tilde{\nu}$, as well as the gradients of these quantities, and the distance from the fluid particle to the surface of the airfoil. (For a complete description of the turbulence model, the reader is referred to the paper by Spalart and Allmaras (1992).) Note that other than the dependence on the distance d from a fluid element to the surface of the airfoil, the turbulence model is entirely local; no global boundary layer quantities, such as the momentum thickness or displacement thickness, are required. Furthermore, as implemented in the present effort, the turbulence model is similar in form to the other conservation equations, and is simply and elegantly solved as an additional conservation equation using an explicit computational fluid dynamic flow solver (see Section 3).

We note that in the present study the flow is assumed to be fully turbulent, i.e., no transition model is used.

2.2. Linearization of Governing Equations

Next, we assume that the unsteadiness in the flow is induced by a small harmonic motion of the airfoils with frequency ω and interblade phase angle σ. Therefore, the unsteadiness in the flow will be a small harmonic perturbation about a mean, but nonuniform, background flow, and the Navier–Stokes equations can be linearized. Hall & Clark (1993) have shown that to improve the accuracy of a time-linearized flow solver, one should make use of strained coordinates. Thus, we make the coordinate transformation given by

$$x(\xi,\eta,\tau) = \xi + f(\xi,\eta)e^{j\omega\tau} \tag{15}$$

$$y(\xi,\eta,\tau) = \eta + g(\xi,\eta)e^{j\omega\tau} \tag{16}$$

$$t(\xi,\eta,\tau) = \tau \tag{17}$$

Here, f and g are small perturbation functions chosen in such a way that in the strained coordinate system, the airfoils appear to be stationary. Said another way, the coordinates ξ,η are attached to the moving airfoil. Within the blade passage, we require that the unsteady grid motion functions f and g vary smoothly.

Next, we decompose the unsteady solution into a steady part, plus a small-perturbation harmonic part, i.e.

$$\mathbf{U}(\xi,\eta,\tau) = \overline{\mathbf{U}}(\xi,\eta) + \mathbf{u}(\xi,\eta)e^{j\omega\tau} \tag{18}$$

Note that the flow decomposition is defined in the strained coordinate system. Substitution of Eq. (18) into the expression for the flux vector $\mathbf{F}$, and expansion in a first-order perturbation series gives

$$\mathbf{F} = \overline{\mathbf{F}} + \frac{\partial\overline{\mathbf{F}}}{\partial\overline{\mathbf{U}}}\mathbf{u}e^{j\omega\tau} + \mathbf{f}\cdot\nabla\overline{\mathbf{F}}e^{j\omega\tau} + \mathcal{F}e^{j\omega\tau} \tag{19}$$

where $\overline{\mathbf{F}} \equiv \mathbf{F}(\overline{\mathbf{U}},\xi,\eta)$. Also, $\nabla = \{\partial/\partial\xi, \partial/\partial\eta\}^T$ and $\mathbf{f} = \{f,g\}^T$. The first term on the right-hand side of Eq. (19), $\overline{\mathbf{F}}$, represents the mean flux vector. In general, $\overline{\mathbf{F}}$ is a function of the spatial coordinates ξ and η, the mean values of conservation variables $\mathbf{U}$, and gradients of the mean conservation variables. The second term on the right-hand side of Eq. (19), $[\partial\overline{\mathbf{F}}/\partial\overline{\mathbf{U}}]\mathbf{u}e^{j\omega\tau}$, represents a perturbation in the flux vector due to perturbations in the conservation variables themselves. This term will have contributions from both the viscous and inviscid elements of the flux vector. The third term on the right-hand side of Eq. (19), $\mathbf{f}\cdot\nabla\overline{\mathbf{F}}e^{j\omega\tau}$, represents the perturbation in the flux vector due to perturbations in the spatial location of the computational node. The flux vectors in the two-dimensional form of the Navier–Stokes equations do not depend explicitly on ξ and η and, therefore, this term is zero. (However, when using the quasi-three-dimensional form of the governing equations, the flux terms *do* depend explicitly on ξ and η, and this term would be nonzero.) Finally, the fourth term on the right-hand side of Eq. (19), $\mathcal{F}e^{j\omega\tau}$, represents the perturbation in the flux vector due to the straining of the computational grid that occurs when df or dg are non-zero. Because the mean solution is attached to the computational grid, straining the computational mesh coordinates induces stresses in the fluid. Only elements of the flux vector that depend on flow gradients (i.e., shear stress, heat conduction, and turbulence model source terms) will contribute to this term. This last term may be neglected if the grid motion is rigid body translation and/or rotation in the vicinity of boundary layers, separated regions, and wakes (Clark & Hall, 1995).

3

The remaining flux and source vectors are similarly expanded in perturbation series, so that

$$\mathbf{G} = \overline{\mathbf{G}} + \frac{\partial \overline{\mathbf{G}}}{\partial \overline{\mathbf{U}}} \mathbf{u} e^{j\omega\tau} + \mathbf{f} \cdot \nabla \overline{\mathbf{G}} e^{j\omega\tau} + \mathcal{G} e^{j\omega\tau} \qquad (20)$$

$$\mathbf{S} = \overline{\mathbf{S}} + \frac{\partial \overline{\mathbf{S}}}{\partial \overline{\mathbf{U}}} \mathbf{u} e^{j\omega\tau} + \mathbf{f} \cdot \nabla \overline{\mathbf{S}} e^{j\omega\tau} + \mathcal{S} e^{j\omega\tau} \qquad (21)$$

Substitution of these perturbation series into the conservation equations described by Eqs. (1) and (2) and grouping terms of equal order in the perturbation quantities yields the zeroth-order mean flow equations,

$$\oint_{\partial\mathcal{D}} (\overline{\mathbf{F}} \, d\eta - \overline{\mathbf{G}} \, d\xi) - \iint_{\mathcal{D}} \overline{\mathbf{S}} \, d\xi d\eta = 0 \qquad (22)$$

and the first-order time-linearized unsteady flow equations,

$$\iint_{\mathcal{D}} \left(j\omega \mathbf{I} - \frac{\partial \mathbf{S}}{\partial \mathbf{U}} \right) \mathbf{u} \, d\xi d\eta + \oint_{\partial\mathcal{D}} \left(\frac{\partial \overline{\mathbf{F}}}{\partial \overline{\mathbf{U}}} \mathbf{u} d\eta - \frac{\partial \overline{\mathbf{G}}}{\partial \overline{\mathbf{U}}} \mathbf{u} d\xi \right)$$

$$= - \iint_{\mathcal{D}} \left(j\omega \overline{\mathbf{U}} - \overline{\mathbf{S}} \right) (d\xi dg + d\eta df) + \iint_{\mathcal{D}} \mathbf{f} \cdot \nabla \overline{\mathbf{S}} d\xi d\eta$$

$$+ \oint_{\partial\mathcal{D}} \left[\left(j\omega f \overline{\mathbf{U}} - \mathbf{f} \cdot \nabla \overline{\mathbf{F}} - \mathcal{F} \right) d\eta - \left(j\omega g \overline{\mathbf{U}} - \mathbf{f} \cdot \nabla \overline{\mathbf{G}} - \mathcal{G} \right) d\xi \right]$$

$$- \oint_{\partial\mathcal{D}} \left[\overline{\mathbf{F}} dg - \overline{\mathbf{G}} df \right] \qquad (23)$$

where $\mathbf{I}$ is the identity matrix. Equation (23) has been arranged so that terms that are homogeneous in $\mathbf{u}$ appear on the left-hand side, and inhomogeneous source terms appear on the right-hand side.

From Eq. (22), it is apparent that the mean flow is independent of the unsteady perturbation flow and grid motion. The perturbation flow, on the other hand, depends on the steady flow in two ways. First, the time-linearized Navier-Stokes equations are linear, inhomogeneous, variable coefficient differential equations. The variable coefficients (mean flow Jacobians) are a function of the mean flow field. Second, the inhomogeneous terms of Eq. (23) are also functions of the mean flow field as well as the prescribed grid motion. Thus, the general solution procedure is to first compute the mean flow. Then, with the mean flow solution known, one forms the Jacobians appearing on the left-hand side, and the inhomogeneous terms on the right-hand side of Eq. (23), and solves the resulting time-linearized Navier-Stokes equations.

Finally, we note that we fully linearize *all* terms in the the governing equations, including Sutherland's viscosity law, the Spalart-Allmaras turbulence model, and the artificial viscosity model used to capture shocks (see Section 3.2). Our experience indicates that simply "freezing" the turbulence model, that is using the steady value of the eddy viscosity in the unsteady analysis with no unsteady perturbation in the viscosity due to the unsteady solution, produces physically incorrect solutions.

2.3. Boundary Conditions

For the steady flow problem, the total pressure, total density, and tangential velocity are prescribed at the upstream far-field boundary; the static pressure is prescribed at the downstream far-field boundary. On the airfoil surface, the no-slip condition requires that the velocity be zero. We also require boundary conditions for the turbulence model. At the upstream far-field boundary, the mean flow turbulence $\overline{\nu}$ is prescribed to be a small but nonzero number, just large enough to "seed" the flow with a small amount of turbulence. On the airfoil surface, we require that $\overline{\nu}$ be zero, because the turbulent viscosity must go to zero at the surface. Finally, the flow is required to satisfy periodicity, i.e.,

$$\overline{\mathbf{U}}(\xi, \eta + G) = \overline{\mathbf{U}}(\xi, \eta) \qquad (24)$$

where G is the blade-to-blade gap.

Similarly, for the unsteady time-linearized flow solution, we require that the flow be periodic with interblade phase angle σ, i.e.,

$$\mathbf{u}(\xi, \eta + G) = \mathbf{u}(\xi, \eta) e^{j\sigma} \qquad (25)$$

An unsteady no-slip condition must also be specified on the airfoil surface. Toward that end, let the vector $\mathbf{R}(s, \tau)$ describe the position of the airfoil surface where s is the distance along the airfoil surface. Because the motion of the airfoil is small and harmonic, we may write that

$$\mathbf{R}(s, \tau) = \overline{\mathbf{R}}(s) + \mathbf{r}(s) e^{j\omega\tau} \qquad (26)$$

Substitution of Eq. (26) into the no-slip condition and collection of first-order terms gives the unsteady no-slip equation

$$\mathbf{v}(s) = j\omega \mathbf{r}(s) \qquad (27)$$

where $\mathbf{v}$ is the perturbation velocity on the airfoil surface.

Finally, for the unsteady flow, we require that outgoing acoustic, vortical, and entropic waves pass through the far-field boundary without reflection. This is equivalent to requiring that there be no incoming waves at the far-field boundary.

3. NUMERICAL IMPLEMENTATION
3.1. Computational Grid

For the present investigation, we use a block-structured grid topology (see Fig. 1). An O-grid is generated around the airfoil so that grid nodes can be concentrated in viscous regions near the airfoil without wasted grid resolution in the far-field region. In the far-field, an H-grid is used because, in this region, one would like a nearly uniform grid to resolve acoustic waves. The grid is generated numerically using the elliptic grid generation technique of Thomas and Middlecoff (1980) with modifications to generate grids with periodic boundaries required for modelling turbomachinery cascades. Inhomogeneous "source" functions are used to cluster grid points near the airfoil surface and provide control over grid orthogonality. A typical computational grid generated using this technique is shown in Fig. 2.

Similarly, a linearized elliptic grid generation technique has been developed to generate the unsteady grid motion functions f and g
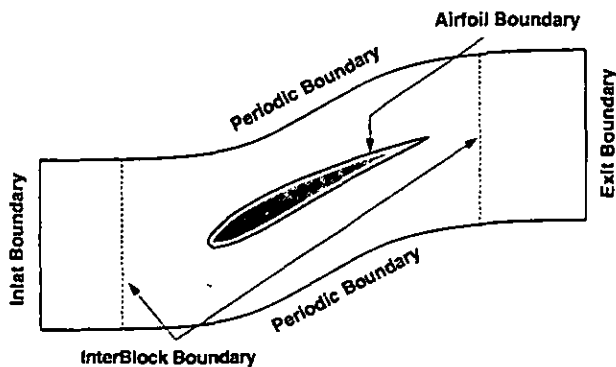
4

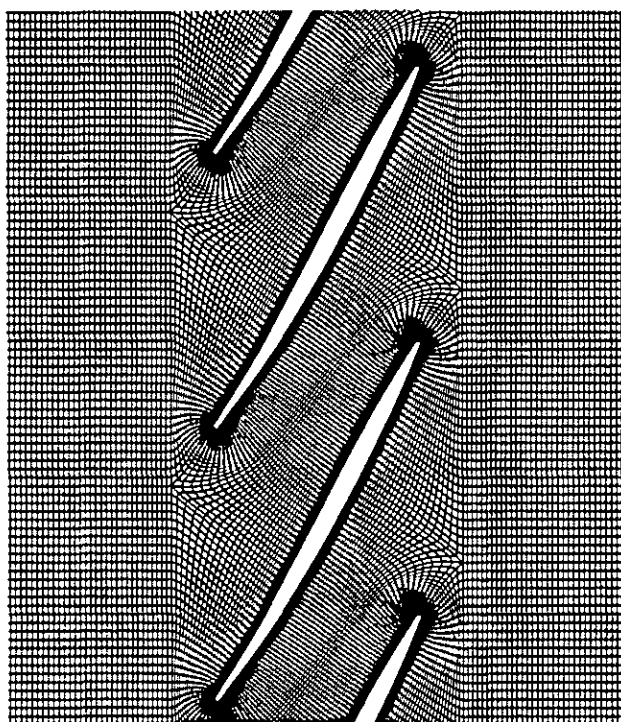**Figure 1: Identification and location of numerical boundary types in computational domain.**

Figure 2: Typical computational grid generated for experimental fan blade (Buffum et al., 1996). Multiple passages are shown for clarity.

required for flutter calculations. The boundary conditions on f and g are that the motion of the grid be equal to the displacement of the airfoil at the surface of the airfoil, and that the motion of the grid be equal to zero on the periodic and far-field boundaries.

3.2. Numerical Integration Scheme

For numerical integration of Eqs. (22) and (23), we add a pseudo-time term to the nonlinear mean and time-linearized unsteady Navier–

Stokes equations, as suggested by Ni and Sisto (1976), so that

$$\frac{d}{d\tau} \iint_{\mathcal{D}} \mathbf{U} d\xi d\eta + \oint_{\partial \mathcal{D}} (\mathbf{F}\, d\eta - \mathbf{G}\, d\xi) = \iint_{\mathcal{D}} \mathbf{S} d\xi d\eta \quad (28)$$

and

$$\frac{d}{d\tau} \iint_{\mathcal{D}} \mathbf{u} d\xi d\eta + \iint_{\mathcal{D}} \left(j\omega \mathbf{I} - \frac{\partial \mathbf{S}}{\partial \mathbf{U}} \right) \mathbf{u}\, d\xi d\eta$$
$$+ \oint_{\partial \mathcal{D}} \left(\frac{\partial \mathbf{F}}{\partial \mathbf{U}} \mathbf{u} d\eta - \frac{\partial \mathbf{G}}{\partial \mathbf{U}} \mathbf{u} d\xi \right) = \mathbf{b} \quad (29)$$

where $\mathbf{b}$ represents the right-hand side of Eq. (23). The addition of the time-dependent terms, the first term on the left of Eqs. (28) and (29), enables us to solve these equations using conventional time marching algorithms. The equations are advanced in pseudo time until the conservation variables reach their steady state values. Hence, the time derivative terms introduced into Eqs. (28) and (29) are driven to zero, and the original steady nonlinear and unsteady linearized Navier-Stokes equations are recovered.

To solve Eqs. (28) and (29), we have implemented a modified version of an explicit finite-volume Lax-Wendroff scheme (Ni, 1982; Saxer, 1992; Davis et al., 1987; Clark, 1998). All spatial derivatives used to evaluate the viscous shear stresses, heat fluxes, etc., are centered differences and are second-order accurate in space. A combination of second and fourth-order smoothing is used to capture shocks (for transonic flows) and eliminate spurious sawtooth modes from the solution (Holmes & Connell, 1989). Because only the steady state values of the mean and perturbation flow are required, there is no need to advance the equations time accurately. Thus, we accelerate convergence using local time stepping and multiple grid acceleration techniques.

3.3. Unsteady Far-Field Boundary Conditions

Because the computational domain must be finite in extent, non-reflecting far-field boundary conditions are applied at the inflow and outflow boundaries to prevent spurious reflections of outgoing pressure, entropy, and vorticity waves. The development of highly accurate nonreflecting boundary conditions continues to receive much attention in the literature. In the present study, we use the Fourier mode decomposition technique developed for time-linearized Euler equations (Hall & Crawley, 1989; Giles, 1990; Hall et al., 1993). If the far-field steady flow is uniform and inviscid, then the unsteady pressure, vorticity, and entropy waves (eigenmodes) will be Fourier modes in the circumferential direction. Each wave (eigenmode) will have a corresponding wavenumber (eigenvalue). The direction of propagation of a given wave is determined by the wavenumber and the corresponding dispersion relation. Thus, at each iteration of the flow unsteady flow solver, the time-linearized solution is Fourier transformed in the circumferential direction to determine the amount of each incoming and outgoing wave present in the solution. For flutter problems, all waves should originate inside the domain. Therefore, the incoming waves are set to zero. The remaining waves are converted back to conservation variables, and inverse Fourier transformed to obtain the solution along the far-field boundary.
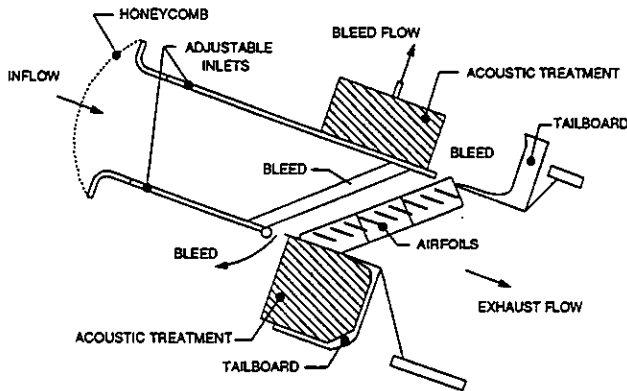
5

Figure 3: NASA Lewis oscillating cascade facility.

To apply the Fourier decomposition technique, two simplifying assumptions are implicitly made. First, we assume that unsteady viscous forces may be neglected. This assumption is valid since the waves that persist over long distances are long wavelength disturbances for which spatial derivatives, and hence viscous forces, are small. Second, we assume that the mean flow in the far field is uniform. This is clearly not true in the downstream region where a substantial velocity defect exists in the steady viscous wake. In fact, small reflections do occur, especially in the vicinity of the wake. However, these reflections tend to have short wavelengths, and thus are acoustically cut off. Any reflections tend to decay rapidly as they propagate upstream and, therefore, have little effect on the solution in the vicinity of the airfoil.

4. COMPUTATIONAL RESULTS

This section presents a flutter stability analysis for a tip section of a low aspect ratio fan blade. The influence of frequency, incidence and flow separation on the aeroelastic stability of the cascade is investigated. Numerical solutions from the present method are compared to experimental data and numerical results obtained from a nonlinear, time-accurate time-marching analysis.

4.1. Benchmark Flutter Data

In this paper, we compare the results of our unsteady time-linearized Navier-Stokes analysis to a set of data recently obtained in the NASA Oscillating Cascade Facility (Buffum et al., 1996). The NASA Lewis Oscillating Cascade Facility (see Fig. 3) is a linear cascade wind tunnel capable of inlet flow speeds approaching Mach 1.0. The tunnel has a high-speed airfoil drive system capable of oscillating the cascaded airfoils in a torsional motion at prescribed interblade phase angles with realistic values of reduced frequency.

The airfoils used in the experiment have a cross section similar to that found in the tip region of modern low aspect ratio fan blades. The airfoil section was designed using the Pratt & Whitney compressor aerodynamic design system. Loading levels, losses, solidity and stagger angle are representative of current design practices, although Mach numbers are somewhat smaller. The aerodynamic chord of
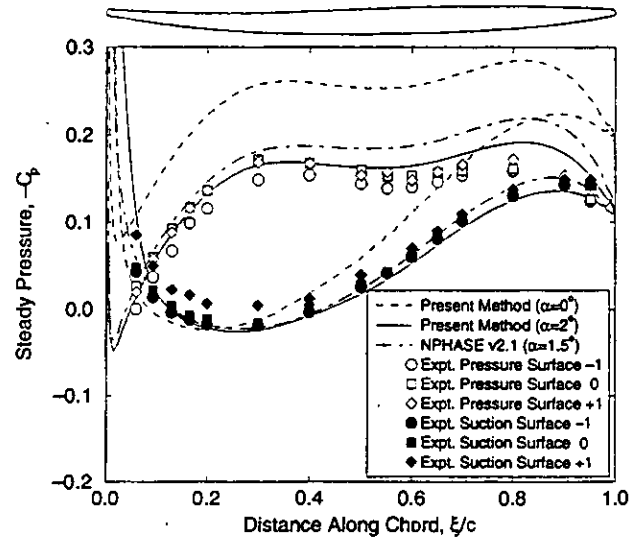

Figure 4: Steady pressure distribution on airfoil surfaces of Buffum cascade. M = 0.2, β_1 = 60°, Re = 380,000.

the airfoil c is 8.90 cm. The airfoils have a maximum thickness of 4.8 percent of the chord, with the maximum thickness located at 62.5 percent of the chord. The linear cascade has nine airfoils set at a stagger angle γ of 60° and a solidity of 1.52. Pressure taps are distributed on several of the airfoil surfaces to measure both steady and unsteady pressure distributions.

Buffum et al. (1996) measured the unsteady aerodynamic response of the airfoils pitching about their midchords for several combinations of steady Mach number and incidence, and unsteady reduced frequency and interblade phase angle. In this paper, we compare the present time-linearized Navier-Stokes analysis to data obtained at two operating conditions, a low-speed low-incidence case, and a low-speed high-incidence case. The later case is representative of operating conditions conducive to stall flutter.

4.2. Low-Speed, Low-Incidence Flutter

The first operating condition considered corresponds to an inlet Mach number M_∞ of 0.2, an inflow angle β_1 of 60° (0° of incidence measured with respect to the chord line), and a Reynolds number Re based on chord of 380,000. At this low-incidence flow condition, viscous effects are thought to be insignificant because the flow remains attached over most of the airfoil and the boundary layers are thin. Figure 4 shows the experimentally measured steady surface pressure data for this case along with the numerical results obtained using the present method ($C_p = (p - p_\infty)/(\rho_\infty U_\infty^2)$). The computational grid used here and throughout the paper unless otherwise noted contained 129×33 nodes in the O-grid region, and 33×33 nodes in the upstream and downstream H-grid regions. The different symbol types in Fig. 4 correspond to data acquired from different airfoils in the cascade. All three instrumented blades are in fair agreement with one another, indicating that reasonable steady
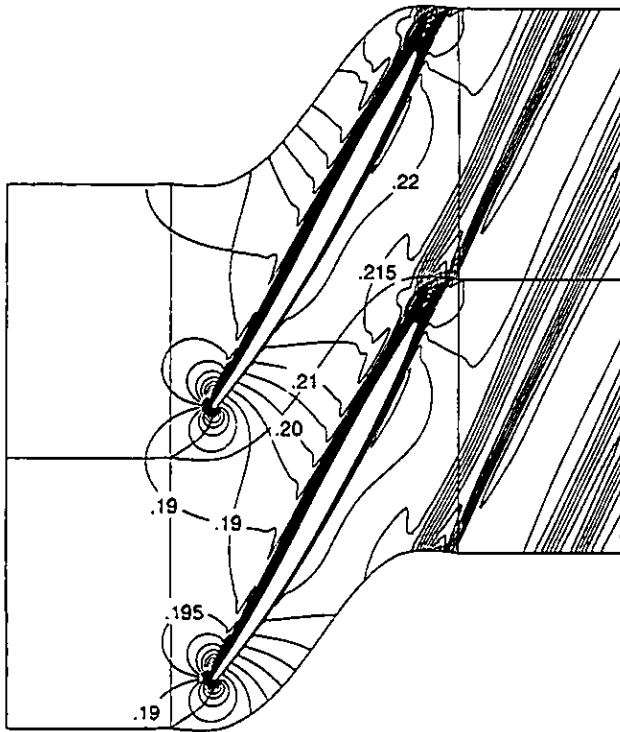
6

Figure 5: Steady Mach contours in blade passages of Buffum cascade. M = 0.2, β_1 = 62°, Re = 380,000.

passage-to-passage periodicity has been obtained in the experiment. The dashed line corresponds to the steady solution computed using the present method for an inflow angle of 60°. The predicted surface pressure distribution has a similar shape to the data, but the pressure levels are not well predicted. By adjusting the inflow angle β_1 to 62°, the surface pressure distribution, denoted now by the solid line, more closely agrees with the experimental results. As errors in the measurement of the cascade stagger angle and/or inflow angle may occur that can substantially alter the steady pressure distribution, it is not unreasonable to adjust the numerically prescribed inflow angle to obtain a closer match to the steady experimental data. Note that with the 2° adjustment, the overall agreement between the present method and the experimental data is quite good.

Also shown in Fig. 4 is the steady pressure distribution computed by Capece (1998) using NPHASE, a fully nonlinear time-accurate time-marching computational model for predicting two-dimensional, nonlinear, unsteady flows through vibrating cascades. NPHASE uses an implicit, cell-centered, finite-volume algorithm based on Roe's approximate Riemann solver. The Baldwin-Lomax (1978) turbulence model is used to compute the eddy viscosity. A detailed description of the NPHASE algorithm is given by Ayre and Verdon (1994). Capece found that the best match to the experimental data was obtained by NPHASE with a prescribed inflow angle of 61.5°. While the overall agreement is good, the pressure on the suction surface of the airfoil is slightly under predicted by NPHASE.
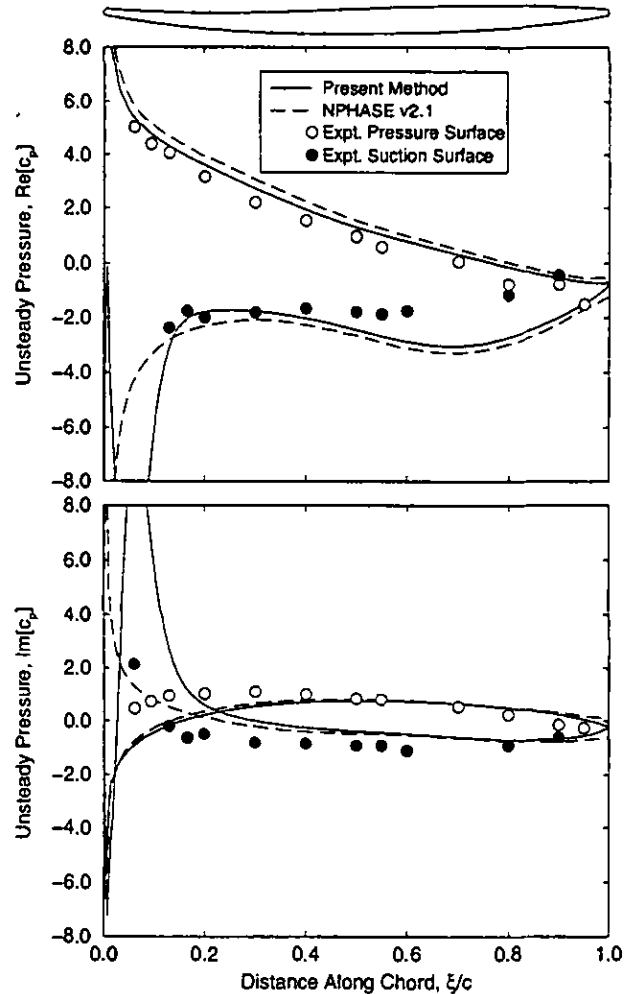

Figure 6: Unsteady pressure distribution on pitching airfoil surfaces of Buffum cascade. M = 0.2, β_1 = 62°, Re = 380,000, k = 1.2, σ = 180°.

Figure 5 shows the steady Mach number contours for this low-speed low-incidence case computed using the present steady Navier–Stokes analysis. The boundary layers are seen to be relatively thin, although on the suction surface there is a small separation bubble near the leading edge – the flow re-attaches approximately 5 percent of the chord downstream of the leading edge – that causes an immediate thickening of the suction surface boundary layer.

Having computed the steady flow, we next consider the unsteady flow arising from torsional vibrations of the airfoils in cascade. For this example, the airfoils in the cascade pitch about their midchords with an interblade phase angle σ of 180° and a reduced frequency $k \equiv \omega c/U_\infty$ of 1.2. The amplitude of torsional vibration α is 1.2°, an amplitude typical of that observed in actual flutter. As with the steady flow calculations, the unsteady flow computations were performed using a single blade passage regardless of interblade phase angle.
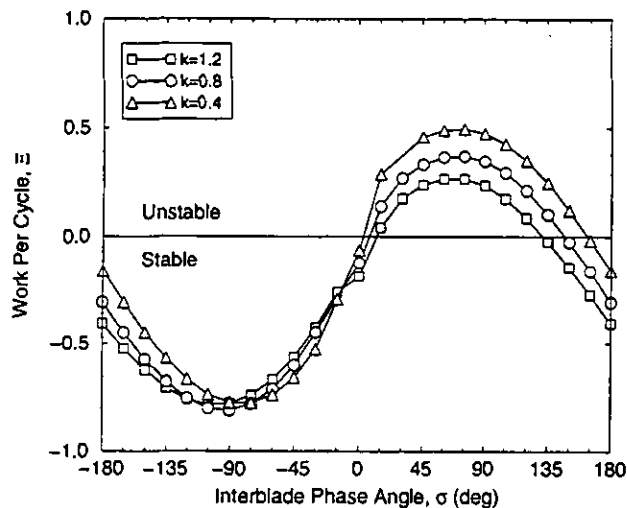
7

Figure 7: Aerodynamic work per cycle due to pitching motion of airfoils for three reduced frequencies. M = 0.2, $\beta_1 = 62°$, Re = 380,000.

Figure 8: Magnitude of pitching moment influence coefficients for three reduced frequencies. M = 0.2, $\beta_1 = 62°$, Re = 380,000.

Shown in Fig. 6 is the computed unsteady real (in-phase) and imaginary (out-of-phase) parts of the unsteady surface pressure predicted using the present time-linearized Navier–Stokes analysis. Also shown for comparison is the experimental data, together with the results of the NPHASE computational model. (The unsteady pressures have been nondimensionalized by $\rho_\infty V_\infty^2 \alpha$.) Unsteady pressure levels predicted by the present time-linearized method are in reasonably good agreement with the experimental data of Buffum et al. (1996), as are the NPHASE results. The largest differences between the two computational solution solutions are near the leading edge of the suction surface.

Next, for this steady operating condition and reduced frequency of torsional vibration, the unsteady aerodynamic moment and work per cycle were computed for a range of interblade phase angles σ and reduced frequencies k. Results for three different reduced frequencies are shown in Fig. 7 for interblade phase angles σ ranging from $-180°$ to $+180°$. Shown is the aerodynamic work done on the blade per vibration cycle Ξ as a function of interblade phase angle σ. As defined in the present effort, if the work per cycle is positive, then the unsteady aerodynamic loads (in the absence of any mechanical damping) result in the aeroelastic instability of flutter. From this figure, we conclude that over a range of interblade phase angles σ from $0°$ to $165°$ the system is aeroelastically unstable. Note, however, that increasing the reduced frequency k has a stabilizing influence on the system in two ways. First, as the frequency is increased, the range of unstable interblade phase angle decreases. Second, the maximum work per cycle for each reduced frequency is reduced. This is consistent with industrial design experience with unstalled flutter, i.e., that increasing the reduced frequency generally has a stabilizing influence on unstalled torsional flutter.

Shown in Fig. 8 is the magnitude of the (complex) unsteady aerodynamic moment in influence coefficient form. The influence coef-
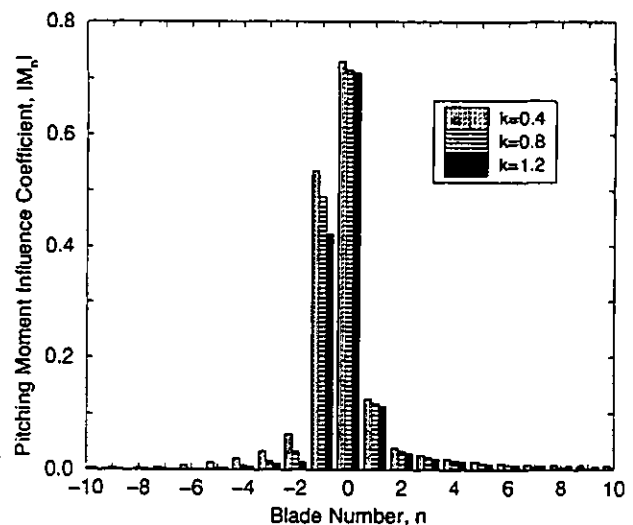
ficients are obtained by performing a discrete Fourier transform on the unsteady moment as a function of interblade phase angle. The result is a measure of the influence of the individual blades on a reference blade. Thus, the blade index corresponding to $n = 0$ describes the moment produced on the reference blade due to vibration of the reference blade itself. The $n = 1$ coefficient indicates the moment produced on the reference blade due to a unit vibration of the neighboring blade on the suction side of the reference airfoil, and so on. For this example we note that the $n \geq 2$ coefficients are relatively small. Physically, this means that only the reference blade and its two nearest neighbors significantly influence the reference blade. Experimentally, this implies that good unsteady passage-to-passage periodicity can be obtained using the nine-bladed NASA Lewis oscillating cascade facility.

4.3. Low-Speed, High-Incidence Flutter

Next, we consider the case where the inlet Mach number M_∞ is 0.2 and the Reynolds number Re is 380,000 as before, but the experimentally reported inflow angle β_1 is now $70°$. Figure 9 shows the computed steady surface pressure distribution computed using the present method along with the experimental data for this case. As before, all three instrumented blades are in good agreement with one another indicating that steady passage-to-passage periodicity has been maintained in the experiment. The solid line corresponds to the steady solution obtained using the present method for an inflow angle of $69°$. Again, the inflow angle has been adjusted slightly to obtain a mean flow solution more closely in agreement with the experimental data. The one area where the present method does not match the data very well is in the leading edge region of the suction surface. A nearly constant pressure region is experimentally observed over the first 20 percent of the chord. The present method, however, shows a monotonically increasing pressure rise. This minor disagreement
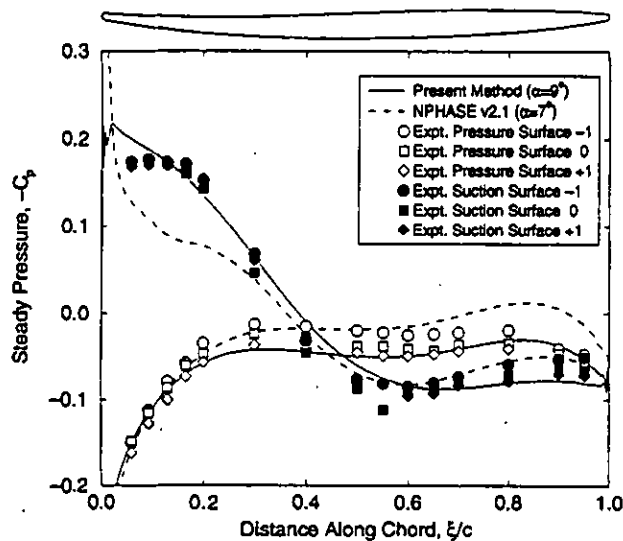
8

Figure 9: Steady pressure distribution on airfoil surfaces of Buffum cascade. $M = 0.2$, $\beta_1 = 70°$, Re = 380,000.

between the data and the present method arises because we assume that the flow is fully turbulent, whereas the actual flow is likely laminar, transitioning to turbulent in this region. This hypothesis has been verified in numerical studies with a potential/boundary layer interaction code (Epureanu et al., 1999). Finally, the dashed line shown in Fig. 9 shows the steady surface pressures distribution computed using NPHASE. The best data match by NPHASE occurred when the inflow angle was 67°.

Figure 10 shows the predicted steady Mach contours for this high incidence case. Note the large separated region that extends from the suction surface leading edge to approximately the airfoil's midchord. Also note that the airfoil wakes are much thicker than those predicted for the low incidence configuration (see Fig. 5). To visualize experimentally this high incidence flow, Buffum coated an airfoil's surface with an oil-pigment mixture. At 10° incidence, separation from the suction surface was observed. The largest separated region was found to exist at the midspan where the flow was observed to separate from the leading edge and re-attach at 40 percent chord. The separated region predicted by the present method is slightly larger, extending over approximately 50 percent of the chord.

Figure 11 shows a comparison between the predicted unsteady surface pressures using both numerical algorithms and experimental data. As before, the unsteady pressures have been nondimensionalized with $\rho_\infty V_\infty^2 \alpha$. The computed imaginary part of the unsteady surface pressure predicted by the present linearized Navier–Stokes method method is in excellent agreement with the experimental data. The computed real part does not agree as well, but is qualitatively in agreement with the experiment. Surface pressure predictions provided by NPHASE, on the other hand, agree with the experimental data on the pressure surface, but large differences in the unsteady surface pressure are observed between NPHASE. It may be that
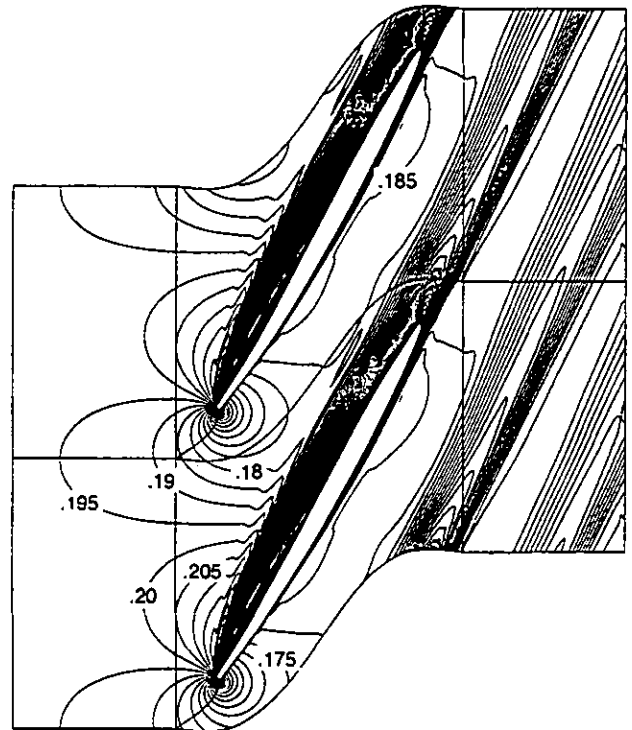

Figure 10: Steady Mach contours in blade passages of Buffum cascade. $M = 0.2$, $\beta_1 = 69°$, Re = 380,000.

the Baldwin-Lomax turbulence model used by NPHASE is not well suited for massively separated flows.

Figure 12 shows the steady and unsteady pressure distributions computed using the present method using three different computational grids, a coarse grid (65×17 nodes in the O-grid region), a medium resolution grid (129×33 nodes), and a fine grid (257×65 nodes). Although some differences in the solutions are observed, especially on the suction surface, the medium and fine grid solutions are in very good agreement indicating the solution is nearly grid converged.

Finally, as before, unsteady flow calculations were performed over a range of frequencies and interblade phase angles. Figure 13 shows the aerodynamic work per cycle Ξ as a function of interblade phase angle σ. From this figure, we conclude that over a range of interblade phase angles ranging from 0° to 165° the system is aeroelastically unstable. Note the strong effect of increased frequency on the system's stability. As before, increasing the reduced frequency has a stabilizing influence on the aeroelastic system in that the range of unstable interblade phase angles diminishes as the frequency of vibration increases. However, the peak work per cycle actually increases as the frequency of vibration increases from $k = 0.4$ to $k = 0.8$. This result may explain in part why increasing blade stiffness has not always been an effective strategy for eliminating observed stall flutter.

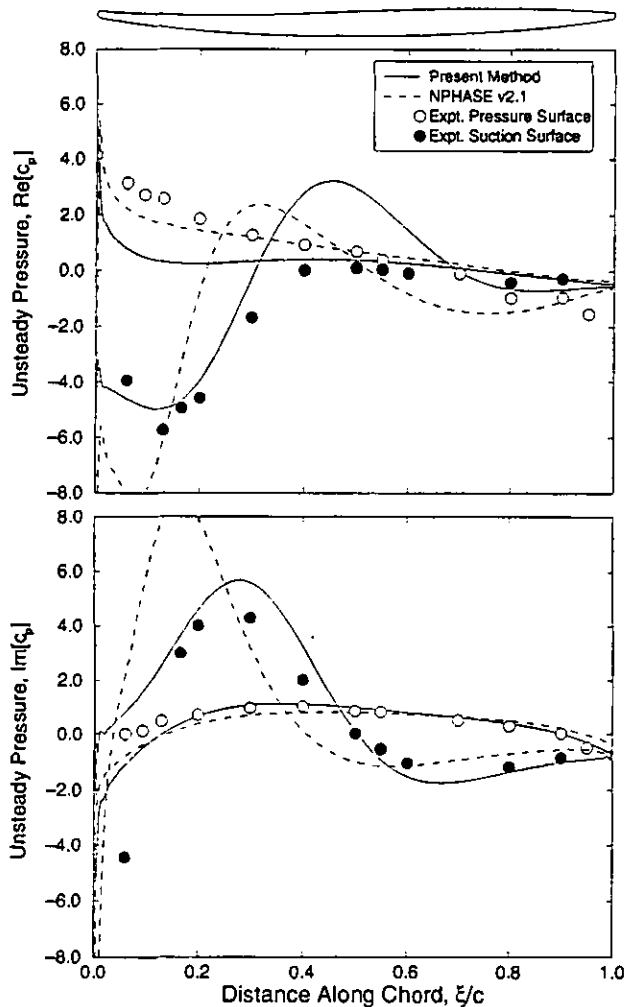Finally, Fig. 14 shows an estimate of the cascade influence co-

9

Figure 11: Unsteady pressure distribution on pitching airfoil surfaces of Buffum cascade. M = 0.2, β_1 = 69°, Re = 380,000, k = 1.2, σ = 180°).

Figure 12: Steady and unsteady pressure distribution on airfoil surfaces of Buffum cascade for various grid resolutions. M = 0.2, β_1 = 69°, Re = 380,000, k = 1.2, σ = 180°).

efficients. Interestingly, there is much more participation by distant neighboring blades in this high incidence configuration than in the low-incidence case. The influence coefficient corresponding to blade indices ±4 are still large when compared to the blade's self influence coefficient. This may indicate that the mechanisms of stall flutter are fundamentally different than those of unstalled flutter. Furthermore, the NASA Lewis oscillating cascade facility, which has just nine fan blades, may not have enough airfoils to ensure unsteady passage-to-passage periodicity.

4.4. Computational Efficiency

One advantage of a time-linearized analysis, often cited by proponents of this modelling strategy, is its computational efficiency compared to conventional time-accurate, time-marching algorithms. Because the governing equations are solved in the frequency domain, conventional steady-st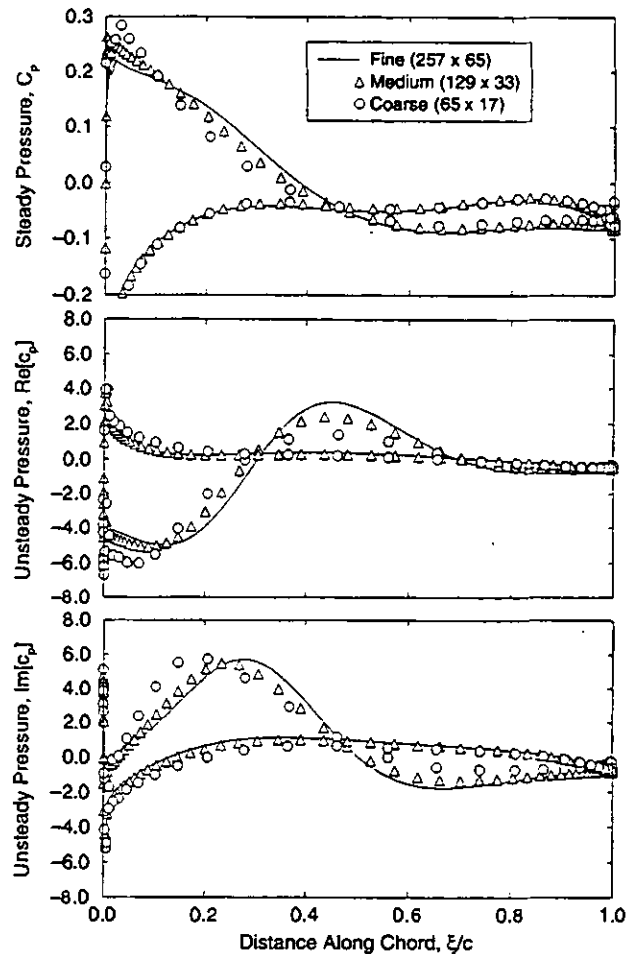ate acceleration techniques may be used to speed convergence. In addition, the use of complex periodicity conditions allows one to compute the unsteady flow using a computational grid spanning a single blade passage, regardless of the interblade phase angle, greatly reducing the number of computational grid points required.

For example, for the low-speed high-incidence example reported in Section 4.3, the computations were performed on a single processor Silicon Graphics workstation equipped with an R10000 processor operating at 195 MHz. The steady code required 4341 iterations to converge six orders of magnitude, and 42 minutes of CPU time. the unsteady analysis for k = 1.2 and σ = 180° required 8378 iterations to converge, and 161 minutes of CPU time. These times are, of course, only representative, and will vary with Mach number, reduced frequency, interblade phase angle, Reynolds number, etc. Nevertheless, a single unsteady calculation requires on the order of just 3.8 times as much computational time as the corresponding steady flow calculation. Thus, the present linearized analysis requires one to two orders
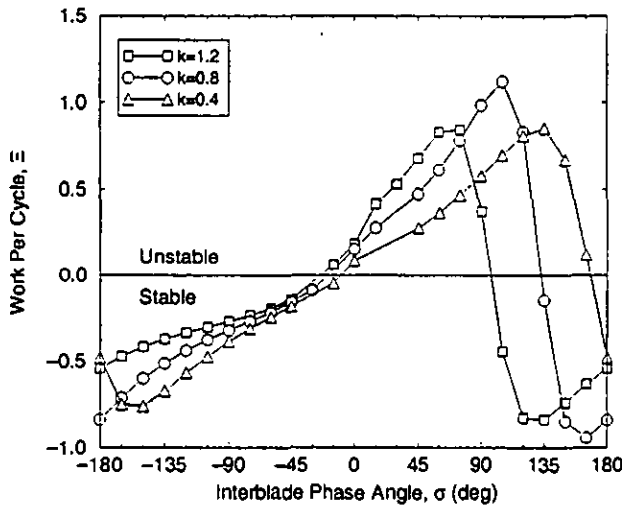
10

Figure 13: Aerodynamic work per cycle due to pitching motion of airfoils for three reduced frequencies. M = 0.2, β_1 = 69°, Re = 380,000).
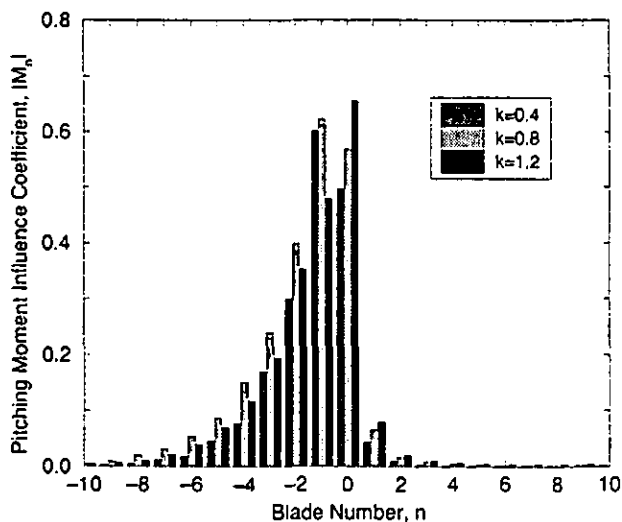

Figure 14: Magnitude of pitching moment influence coefficients for three reduced frequencies. M = 0.2, β_1 = 69°, Re = 380,000.

of magnitude less computational time to converge than conventional time-accurate, time-marching algorithms. (We would also note that the unsteady calculations are performed using complex arithmetic, which simplifies code development, but also degrades computational performance. It is possible to write the unsteady code using only real arithmetic, improving somewhat the computational efficiency.)

5. CONCLUDING REMARKS

In this paper, we have presented a novel time-linearized Navier–Stokes computational analysis of stall flutter in cascades. Based on the results obtained to date, we make the following observations.

1. The time-linearized Navier–Stokes analysis is able to model the complex steady and unsteady flow associated with stall flutter, including large separated flow regions. Results of this analysis compare quite well with experimental data of high-incidence stall flutter.

2. The method is computationally efficient making it useful for routine use in aeroelastic design; the computational time required to compute the unsteady flow due to a single mode shape of blade motion at a single frequency and interblade phase angle is of the same order as the time required to compute the background steady flow. Furthermore, results obtained with the present time-linearized Navier–Stokes analysis agree with experimental data as well as predictions obtained using a conventional (and computationally expensive) nonlinear time-domain analysis.

3. Numerical results from the low-speed, incidence-incidence example are consistent with industrial design experience, i.e., that increasing the reduced frequency generally increases aerodynamic damping. The high-incidence results, on the other hand, seem contradictory to standard design practices, as the range of unstable interblade phase angles is reduced by increasing the reduced frequency, but the aerodynamic damping of the least stable interblade phase angle becomes more unstable with increasing reduced frequency. Additional numerical and experimental studies need to be performed to understand this phenomenon.

4. While the present method is two-dimensional, stall flutter in actual turbomachines is likely to be highly three-dimensional with the extent of the separated region varying significantly from hub to tip. Nevertheless, the results presented in this paper demonstrate the feasibility of using a time-linearized Navier–Stokes model to predict stall flutter, and the method should be readily extendable to three dimensions, albeit with an attendant increase in computational requirements.

Before gas turbine engine designers can consistently avoid stall flutter, the underlying mechanisms must be understood. Computationally efficient and experimentally validated models, such as the present time-linearized Navier-Stokes code, are an invaluable tool for studying the aerodynamics of stall flutter.

ACKNOWLEDGMENTS

REFERENCES

Ayre, T. C., and Verdon, J. M., 1994, "Numerical Unsteady Aerodynamic Simulation for Blade Forced Response Phenomena," Wright Laboratory Technical Report, WL–TR–95–2011.

Baldwin, B. S., and Lomax, H., 1978, "Thin Layer Approximation and Algebraic Model for Separated Turbulent Flows," Presented at the 16th AIAA Aerospace Sciences Meeting, AIAA Paper 78–257.

Buffum, D. H., Capece, V. R., King, A. J., and EL-Aini, Y. M., 1996, "Experimental Investigation of Unsteady Flows at Large Incidence Angles in a Linear Oscillating Cascade," AIAA Paper 96–

11

2823.

Capece, V., 1998, "Numerical Investigation of Oscillating Cascade Aerodynamics at Large Mean Incidence," Presented at the 3rd National High Cycle Fatigue (HCF) Conference, San Antonio, Texas February 2–5.

Chi, R. M., and Srinivasan, A. V., 1985, "Some Recent Advances in the Understanding of Turbomachine Subsonic Stall Flutter," *Journal of Engineering for Gas Turbines and Power*, Vol. 107, pp. 408–417.

Clark, W. S., 1998, "Investigation of Unsteady Viscous Flows in Turbomachinery Using a Linearized Navier-Stokes Analysis," Ph.D. Thesis, Duke University.

Clark, W. S., and Hall, K. C., 1995, "A Numerical Model of the Onset of Stall Flutter in Cascades," ASME Paper 95-GT-0377, Presented at the International Gas Turbine and Aeroengine Congress and Exposition, Houston, Texas June 25-29.

Davis, R. L., Ni, R. H., and Carter, J. E., 1987, "Cascade Viscous Flow Analysis Using the Navier-Stokes Equations," *Journal of Propulsion*, Vol. 3, No. 5, pp. 406–414.

Epureanu, B., Hall, K.C., and Dowell, E.H., 1999, "Reduced Order Model of Unsteady Viscous Flows in Turbomachinery Using Viscous-Inviscid Coupling," submitted to *Journal of Fluids and Structures*.

Giles, M. B., 1990, "Nonreflecting Boundary Conditions for Euler Equation Calculations," *AIAA Journal*, Vol. 28, No. 12, pp. 2050–2058.

Hall, K. C., 1993, "Deforming Grid Variational Principle for Unsteady Small Disturbance Flows in Cascades," *AIAA Journal*, Vol. 31, No. 5, pp. 891-900.

Hall, K. C. and Clark, W. S., 1993, "Linearized Euler Predictions of Unsteady Aerodynamic Loads in Cascades," *AIAA Journal*, Vol. 31, No. 3, pp. 540–550.

Hall, K. C., and Crawley, E. F., 1989, "Calculation of Unsteady Flows in Turbomachinery Using the Linearized Euler Equations," *AIAA Journal*, Vol. 27, No. 6, pp. 777–787.

Hall, K. C., and Lorence, C. B., 1993, "Calculation of Three-Dimensional Unsteady Flows in Turbomachinery Using the Linearized Harmonic Euler Equations," ASME *Journal of Turbomachinery*, Vol. 115, pp. 800-809.

Hall, K. C., Lorence, C. B., and Clark, W. S., 1993, "Nonreflecting Boundary Conditions for Linearized Aerodynamic Calculations," Presented at the AIAA 31st Aerospace Sciences Meeting, Reno, NV. AIAA Paper 93–0882.

Holmes, D. G., and Chuang, H. A., 1993, "2D Linearized Harmonic Euler Flow Analysis for Flutter and Forced Response," in *Unsteady Aerodynamics, Aeroacoustics, and Aeroelasticity of Turbomachines and Propellers*, H. M. Atassi, ed., Springer-Verlag, New York, pp. 213-230.

Holmes, D. G., and Connell, S. D., 1989, "Solution of the 2-D Navier–Stokes Equations on Unstructured Adaptive Grids," AIAA Paper 89-1943-CP.

Holmes, D. G., and Lorence, C. B., 1998, "Three-Dimensional Linearized Navier–Stokes Calculations for Flutter and Forced Response," in *Unsteady Aerodynamics and Aeroelasticity of Turbomachines: Proceedings of the 8th International Symposium held in Stockholm, Sweden, 14–18 September 1997*, T. H. Fransson, ed., Kluwer Academic Publishers, Dordrecht, pp. 211–224.

Ni, R. H., and Sisto, F., 1976, "Numerical Computation of Nonstationary Aerodynamics of Flat Plate Cascades in Compressible Flow," *Transactions of the ASME: Journal of Engineering for Power*, Vol. 98, pp. 165–170.

Ni, R. H., 1982, "A Multiple-Grid Scheme for Solving the Euler Equations," *AIAA Journal*, Vol. 20, No. 11, pp. 1565–1571.

Sisto, F., 1987, "Stall Flutter," in *AGARD Manual on Aeroelasticity in Axial-Flow Turbomachines, Vol. 1, Unsteady Turbomachinery Aerodynamics*, M. F. Platzer and F. O. Carta, eds., AGARD-AG-298, ch. 7.

Spalart, P. R., and Allmaras, S. R., 1992, "A One Equation Turbulence Model for Aerodynamic Flows," AIAA Paper, 92–0439.

Saxer, A. P., 1992, "A Numerical Analysis of 3-D Inviscid Stator/Rotor Interactions Using Non-Reflecting Boundary Conditions," Ph.D. Thesis, Department of Aeronautics and Astronautics, Massachusetts Institute of Technology, Cambridge, Massachusetts.

Thomas, P. D., and Middlecoff, J. F., 1980, "Direct Control of the Grid Distribution in Meshes Generated by Elliptic Equations," *AIAA Journal*, Vol. 18, No. 6, pp. 652–656.

Verdon, J. M., 1987, "Linearized Unsteady Aerodynamic Theory," in *AGARD Manual on Aeroelasticity in Axial Flow Turbomachines, Vol. 1, Unsteady Turbomachinery Aerodynamics* (AGARD-AG-298), M. F. Platzer and F. O. Carta, eds., Neuilly sur Seine, France, ch. 2.

Verdon, J. M., and Caspar, J. R., 1982, "Development of a Linear Unsteady Aerodynamic Analysis for Finite-Deflection Subsonic Cascades," *AIAA Journal*, Vol. 20, No. 9, pp. 1259-1267.

Whitehead, D. S., and Grant, R. J., 1981, "Force and Moment Coefficients of High Deflection Cascades," in *Proceedings of the 2nd International Symposium on Aeroelasticity in Turbomachines*, P. Suter, ed., Juris-Verlag, Zurich, pp. 85-127.